The lunar photoelectron sheath: A change in trapping efficiency during a solar storm

W. M. Farrell,[1,4] A. R. Poppe,[2,4] M. I. Zimmerman,[1,3,4] J. S. Halekas,[2,4] G. T. Delory,[2,4] and R. M. Killen[1,4]

Received 28 September 2012; revised 23 April 2013; accepted 25 April 2013.

[1] On the lunar dayside, photoelectrons are quasi-constantly emitted from the Moon's surface and this electron flux acts to typically charge the dayside lunar surface a few volts positive. In arriving at an equilibrium surface potential, the surface will charge to balance the two primary currents: the outgoing photoelectron flux, J_p, against the incoming solar wind electron thermal flux, J_e. In nominal solar wind conditions, $J_p > J_e$ and the surface charges positive, trapping most of the photoelectrons. However, during the passage of a coronal mass ejection (CME), the incoming electron thermal flux, J_e, will quickly change from being less than J_p to being greater than J_p on time scales of ~1–2% of a lunation. Using a set of independently developed particle-in-cell plasma codes, we find at times when $J_p/J_e < 1$, there is substantially less near-surface electrostatic trapping of the photoelectrons due to the reduction of the restraining surface potential. The photoelectron population then has almost direct access to upstream regions. We find that the morphology of the sheath is very different in the CME's dense cool plasma than in the nominal solar wind, with a larger relative portion of the photoelectrons now liberated to propagate upstream into plasma regions ahead of the Moon.

Citation: Farrell, W. M., A. R. Poppe, M. I. Zimmerman, J. S. Halekas, G. T. Delory, and R. M. Killen (2013), The lunar photoelectron sheath: A change in trapping efficiency during a solar storm, *J. Geophys. Res. Planets*, *118*, doi:10.1002/jgre.20086.

1. Introduction

[2] The Sun emits UV and X-ray photonic emission and this energy is directly incident on the lunar surface. In response to the solar energy at small wavelength, the lunar surface emits electrons via the photoelectric effect: Photons with energies greater than the material work function liberate electrons at 1–2 eV from the surface [*Reasoner and Burke*, 1972a, 1972b]. At the subsolar point, this photoelectron current is about four times greater than the nominal thermal flux from the incoming solar wind electrons. The excessive loss of electrons from the surface will cause the interface to charge to a net positive potential (of about +3–5 V) [*Manka*, 1973]. This potential acts to trap the newly emitted photoelectrons to form an electron-rich sheath that covers the dayside surface [*Manka*, 1973; *Stubbs et al*., 2006; *Poppe and Horanyi*, 2010]. However, the solar wind electron thermal flux that controls the photoelectron-restraining surface potential is itself variable and undergoes very large changes especially during a passage of a coronal mass ejection (CME). As we demonstrate herein, this change in solar wind electron flux has the ability to alter the physical nature and trapping efficiency of the photoelectric sheath.

[3] This work is performed as part of the Solar Storm Lunar Atmosphere Modeling (SSLAM) effort organized by NASA's Lunar Science Institute. In SSLAM, the understanding of the lunar plasma/surface/exosphere interactions during an extreme solar storm event is advanced using a set of cross-connected models driven by a common event trigger [*Farrell et al*., 2012]. The event selected for study is the solar storm and CME passage that occurred on 1–3 May 1998.

[4] Direct observations of the photoelectric sheath were made by the Charged Particle Lunar Environment Experiment that detected surface electron fluxes when the Moon was in the geomagnetic tail [*Reasoner and Burke*, 1972a, 1972b; *Feuerbacher et al*., 1972]. The modeling of the lunar photoelectric sheath [*Manka*, 1973; *Nitter et al*., 1998; *Stubbs et al*., 2006] has become more advanced with the use of kinetic particle-in-cell plasma codes. *Poppe and Horanyi* [2010] found that photoelectron emission creates an outward directed E field of approximately +3 V/m from the positive surface, extending out to about 3 m in height. However, they also reported on the development of an opposite E-field region above the sheath where there is the presence of a weaker inward directed E field of 0.1–0.3 V/m extending from 3 m to 30 m in height. This inward directed E is over 30 times larger than the solar wind convection E field of 3 mV/m and thus is a significant electrostatic

[1]NASA Goddard Space Flight Center, Greenbelt, Maryland, USA.
[2]Space Sciences Laboratory, The University of California, Berkeley, Berkeley, California, USA.
[3]Oak Ridge Associated Universities, Oak Ridge, Tennessee, USA.
[4]NASA Lunar Science Institute, NASA Ames Research Center, Moffett Field, California, USA.

Corresponding author: W. M. Farrell, NASA Goddard Space Flight Center, Greenbelt, MD, USA. (William.M.Farrell@nasa.gov)

2169-9097/13/10.1002/jgre.20086

structure. *Halekas et al*. [2012 a, 2012b] discovered the implicit signature of this inward E revealed in the reflected loss cone electrons and anomalous electron beams in dayside regions well upstream of the Moon using electron spectrometers onboard Lunar Prospector (LP) [*Halekas et al*; 2005] and ARTEMIS [*Angelopoulos*, 2011]. The inward directed E field acts to repel a fraction of the inward flowing solar wind electrons and accelerate low-energy electrons (cold sheath electrons) into upstream regions.

[5] A more complete picture is now emerging of the formation of a precursor region found upstream of the Moon [*Poppe and Horányi*, 2010; *Poppe et al*., 2011, 2012; *Halekas et al*., 2011, 2012a, 2012b]: As an interplanetary magnetic field line first comes in contact with the Moon, the nearly isotropic electron population no longer contains its upstreaming/outflowing component due to occulting by the solid body. Compared to the solar wind ions (that are primarily a directed flow inward toward the Moon), there is now a charge imbalance on the connecting field line, with the region above the cold photoelectric sheath containing a net positive charge (density of ions greater than the density of electrons, $n_i > n_e$). In a self-consistent way, the inward directed E field attempts to accelerate or "suck" the cold photoelectrons upstream to compensate for the charge imbalance. The E field also repels part of the original solar wind electron population; again in an attempt to maintain neutrality along the field line. The extent of the non-neutral region in distant upstream regions is surprisingly large (~10–50 m) [*Poppe and Horanyi*, 2010] and may even create a slight net positive potential for some distance along the connecting field line created by the persistent charge imbalance in the upstream precursor region.

[6] This new picture suggests the dayside upstream region of the Moon is far more dynamic than originally envisioned. The conventional wisdom was that solar wind ion and electron populations are fully absorbed at the dayside lunar surface and that little or no plasma-related disturbance (i.e., precursor) propagates upstream in the dispersive plasma medium. The recent Kaguya discovery of reflected solar wind ions [*Saito et al*., 2008] and the LP/ARTEMIS discovery of reflected electrons and beams [*Halekas et al*., 2011, 2012a, 2012b; *Poppe et al*., 2011, 2012] suggest that the upstream portion of the Moon has analogous features to the foreshock region found ahead of the terrestrial bow shock.

[7] The variation of the photoelectric sheath with solar UV conditions was modeled via a one-dimensional particle-in-cell (PIC) electrostatic code by *Poppe and Horanyi* [2010]. Given the large dimension of the lunar surface and the relatively small vertical sheath size, electron flow along a magnetic field line can be reasonably modeled via a 1-D PIC approach. The effect of local topography cannot be included in such a model, and it applies best in the case of a flat surface with a magnetic field oriented quasi-parallel to the surface normal [*Poppe and Horanyi*, 2010]. Their model found a number of new results including the discovery of an inward directed E and the effect of the sheath under varying UV photon intensity. In the latter, they found that the surface E field can increase by ~30% from the nominal UV flux at solar minimum to solar maximum conditions. They also found that during a flare event, the near-surface E field can double from nominal solar minimum conditions.

[8] In this work, we now address another controlling element on the sheath and precursor region: that of the incoming solar wind electron thermal flux. This solar wind electron flux acts at the surface to create a near-surface potential that is in balance with the emitted photoelectric current. During the various phases of a CME passage, this inflowing electron flux will vary greatly, at times becoming comparable to or exceeding the photoelectron current. We demonstrate that the nature of the sheath and its ability to contain/trap the photoelectrons is altered during the CME passage on time scales of a fraction of a lunation. We will be modeling plasma conditions at the lunar surface that have not been examined previously via plasma simulation, thus we use one simulation to provide the foundation for trapping and escape. The additional two models are used to provide critical validation and additional context.

2. Solar Storms in Early May 1998

[9] The solar storm event being considered is that occurring from 1 to 3 May 1998 [*Farrell et al*., 2012]. Specifically, a set of solar flares occurred in late April and early May 1998, releasing a series of CMEs. Near the end of the day on 29 April, an M8 flare occurred in conjunction with an earthward directed CME that was considered geo-effective. Figure 1 shows the solar wind density, temperature, flow speed, and the magnitude of B as measured by upstream plasma monitors (from the Omni data set, see *Farrell et al*. [2012]). We divide up the CME passage into four primary intervals: nominal solar wind, post-shocked warm solar wind, early CME, and late CME. Compared to the nominal solar wind, the post-shocked plasma is about 4 times denser and 3–4 times warmer (in plasma temperature). The early CME plasma is similar in nature to the nominal solar wind, but the late CME plasma is over 10 times denser and 3–5 times cooler. Hence, the plasma environment at the lunar surface is undergoing substantial changes during the CME passage.

[10] Table 1 herein lists the solar wind electron thermal flux to the surface. Since the solar wind ion flux lies well below that of the solar wind electrons, surface current balance and charging are primarily defined by the inflowing solar wind electron thermal flux and outflowing photoelectron surface emission. In a simple sheath, the surface potential varies as the log of J_p/J_e [*Manka*, 1973] making J_p/J_e a key ratio for indexing and comparing our results. For interval 1 (nominal solar wind), the electron thermal current is ~1 $\mu A/m^2$ and lies well below the photoelectron current of ~4 $\mu A/m^2$ at the subsolar point. In this case, $J_p/J_e > 1$ and the surface charges positive and has a positive surface potential that is capable of trapping a large portion of the emitted photoelectrons. In contrast, during the passage of the warm CME post-shocked plasma past the Moon (interval 2) and in the highest density portions of the CME itself (interval 4), $J_p/J_e < 1$ and the incoming electron flux is capable of reducing the positive surface-charge buildup resulting in a greater release of escaping photoelectrons into upstream regions.

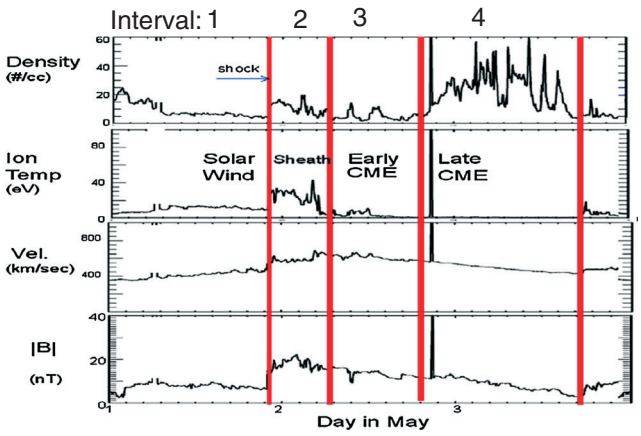

Figure 1. Upstream observations of the 1–3 May 1998 CME passage past the Earth-Moon system. The passage is divided up into four intervals of (1) solar wind, (2) warm post-shocked, plasma, (3) early CME, and (4) late dense CME plasma.

3. Description of Codes

[11] There are three codes that are used in this study. The inclusion of three different codes was an evolutionary process: We first modeled the CME passage by the Moon using one simulation, but the results were different than expected and required validation, especially given that the specific photoelectron and solar wind plasma at the surface had not been modeled before (i.e., investigating very new parameter regimes). Hence, the team used two other codes in their possession to provide that critical validation of photoelectron trapping and escape. While the codes differ in setup and boundaries, the overall results regarding trapping are similar (see more details in section 9).

[12] The primary code featured is that recently published: The *Poppe and Horanyi* [2010] particle-in-cell (PIC) code is a one-dimensional, electrostatic model and traces plasma motion along the surface connecting magnetic field line. The particle populations being modeled include photoelectrons from the lunar surface and solar wind electrons and ions from the ambient plasma. In such a one-dimensional code, there are two boundaries for consideration: an inner boundary (to the left in our figures) and an outer (right) boundary. As described in *Poppe and Horányi* [2010], the inner boundary of the simulation represents the lunar surface and the outer boundary is a closed border that reprocesses any escaping plasma or photoelectrons into solar wind plasma. Photoelectrons are emitted from the lunar surface (left boundary) with a specified velocity distribution (for this work, a $T_{ph} = 2.2$ eV Maxwellian [*Feuerbacher et al.*, 1972]), while solar wind electrons and ions are injected from the outer boundary with plasma conditions consistent with the four intervals of study shown in Figure 1 and described in Table 1 (consistent with the plasma parameters shown in Table 1 of *Farrell et al.* [2012]). We used a simulation ion mass of $m_i = 800m_e$ (m_e is the electron mass), which is sufficiently large enough to capture the supersonic nature of the solar wind protons without rendering the simulation computationally prohibitive. At the simulation start-up, the solar wind plasma inflows from the outer (right) boundary and photoelectrons outflow from the surface (left) boundary to fill up the vacuum region in between the two boundaries. Simulations are run until the solar wind obtains equilibrium with the inner boundary (i.e., the surface) and after reaching this system-level equilibrium, results are obtained and presented. Comparisons between the PIC simulation results and in situ measurements of the plasma environment above the dayside lunar surface in the terrestrial magnetotail have found good agreement and validated several aspects of the code [*Poppe et al.*, 2011, 2012].

[13] To verify and expand the results of the changing morphology of the lunar photoelectric sheath, we compared the first PIC code results to two other 1D PIC codes. Not only do the results provide critical validation, but these other codes also emphasize other unique aspects of the photoelectron beam/solar wind plasma interaction. One of these verification codes was used in the past for studies of electron beams from the space shuttle [*Farrell et al.*, 1989; *Farrell and Goertz*, 1990]. Like *Poppe and Horanyi* [2010], it assumes that the electron flow is in one dimension along the interplanetary B field. It is also assumes a nominal photoelectron current level like that for direct solar radiation incident on the surface at 1 AU and a photon-to-electron efficiency of 0.1 [*Reasoner and Burke*, 1972b], yielding a photoelectron current from the surface of ~4 $\mu A/m^2$ [*Feuerbacher et al.*, 1972; *Manka*, 1973].

[14] The code includes an inner surface-like boundary at the inner (left) edge. Electron beams/photoelectrons are emitted from this boundary with an equal and opposite charge being placed at the boundary to compensate and maintain system-level charge neutrality. At the outer (right) boundary, solar wind electrons and ions are ballistically

Table 1. Parameters Used in the Simulation Study[a]

	Interval 1 Nominal Solar Wind	Interval 2 Post-Shock Plasma	Interval 3 Early CME	Interval 4 Late CME	Interval 3a Early CME With Flare
J_p ($\mu A/m^2$)	4	4	4	4	20
J_e ($\mu A/m^2$)	1	8	1	7	1
J_p/J_e	4	0.5	4	0.6	20
n/n_o	1	4	1	14	1
v_{te}/v_{teo}	1	2	1	0.2	1
Is potential monotonic?	no	yes	no	yes	no
n_s/n_u [PH]	30	2.5	30	2.5	125
n_s/n_u [F]	50	19	50	3	200
n_s/n_u [Z]	100	25	100	6	573

[a]The variable n/n_o and v_{te}/v_{teo} are the applied solar wind density and thermal velocity ratios as compared to the nominal solar wind. The resulting surface-to-upstream photoelectron density ratio, n_s/n_u, for each of the simulation codes (Poppe/Horanyi [PH], Farrell [F], and Zimmerman [Z]) is also presented.

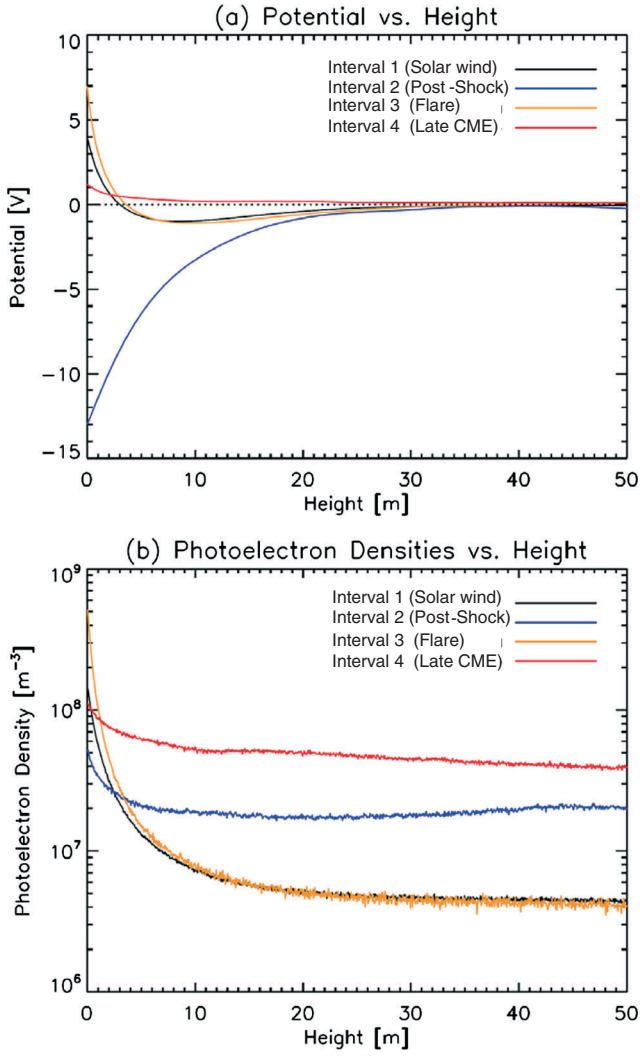

Figure 2. The (a) potential and (b) photoelectron density as a function of height above the lunar surface from the simulation code by *Poppe and Horanyi* [2010].

streaming inward toward the surface at a preset flow velocity (~400 km/s). At the start of the runs, the solar wind plasma occupies a position from the inner boundary out to beyond the outer boundary (~3 times the simulation size). As such, the plasma obtains equilibrium with the surface in a few plasma periods. The code is designed such that when a substantial portion of the photoelectrons has left the simulation via the outer (right) boundary, the simulation is turned off.

[15] A third independent 1-D particle-in-cell simulation developed by M. Zimmerman was run that also allows particles to leave the simulation domain through the outer boundary. The plasma population being simulated is similar to the other two simulations: incoming solar wind electrons and ions and surface-emitted photoelectrons. In this code, the solar wind plasma initially fills the entire system (for a quiet start) and inward moving particles are supplied at a constant rate at the outer boundary to simulate the moonward flowing solar wind. Thus, the code is capable of modeling transient, system-wide responses to abrupt contact of the solar wind with the dayside lunar surface as well as the natural progression to a long-time equilibrium. The electric field at the surface is σ/ε_0, where σ is the accumulated surface charge density and ε_0 is the permittivity of free space, and the electric potential is held at 0 V at the open solar wind boundary. Finally, the grid points were uniformly spaced by $\Delta x = 0.2$ m which was chosen to be less than the photoelectron Debye length of ~1 m and the simulation time step was $\Delta t = 5 \times 10^{-8}$ s to satisfy the Courant condition $\Delta x > v_{\max} \Delta t$ where $v_{\max}$ is the maximum anticipated particle velocity. Values for $v_{\max}$ range on a case-by-case basis, but a typical value is about 3 times the solar wind electron thermal velocity v_{the}, which is greatest during interval 2 at a value of approximately $v_{\text{the}} = 5 \times 10^8$ m/s.

[16] We will initially present the results of the varying solar wind conditions featuring *Poppe and Horanyi* [2010] code. In section 9, we will expand the code description and compare/contrast the results from all three codes.

4. Interval 1: Nominal Solar Wind

[17] Figures 2a and 2b show the equilibrium electrostatic potential and the photoelectron density from the *Poppe and Horanyi* [2010] code as a function of height, respectively, for all four cases considered. The code was applied originally to the case of nominal solar wind and also increased solar radiation, but we now apply this durable code to consider the effect the solar wind electron thermal flux, J_e, on photoelectron emission. The electrostatic potential has an array of morphologies across the four cases, including both positively and negatively monotonic and non-monotonic structures. During this first interval, the Moon was immersed in a near-nominal solar wind flow having $J_p \sim 4\ J_e$. In this time period, the potential is non-monotonic with a minimum around −1 V at 8 m in height and a maximum at the surface of approximately +4 V, similar to previous simulations [*Poppe and Horányi*, 2010].

[18] In Figure 2a, the profile of interval 1(black line) has a positive near-surface potential that is indicative of an outward directed E field capable of trapping/retaining a large portion of the photoelectron beam. For the approximately +4 V surface potential, only the high-energy tail of the 2.2 eV Maxwellian electron distribution can escape to greater altitudes into upstream regions. Between 3 m and ~30 m in altitude, the E field actually becomes slightly negative (the non-monotonic potential) [*Poppe and Horányi*, 2010] which then acts to accelerate these leaking/escaping photoelectrons to near the solar wind electron thermal velocity of ~2000 km/s as they move outward from the surface.

[19] Figure 2b shows the density profile with altitude for the solar wind case, interval 1. In equilibrium, the near-surface density is found to be about 1.2×10^8 electrons/m^3 but exponentially decays to values near 4×10^6/m^3 in the nominal solar wind. If there were no changes in potential (no near-surface potential of +4 V and no negative potential between 3 and 30 m), the outward flowing photoelectron density would be constant at all altitudes; this is due to the uniform motion of electrons from the boundary outward. However, the near-surface positive potential traps a vast number of photoelectrons in the first few meters to create a density enhancement that is 30 times larger than that found in the distant upstream region in the solar wind. In the first 3 m above the surface, where the electric field, E, is positive, the density enhancement relative to distant regions is due

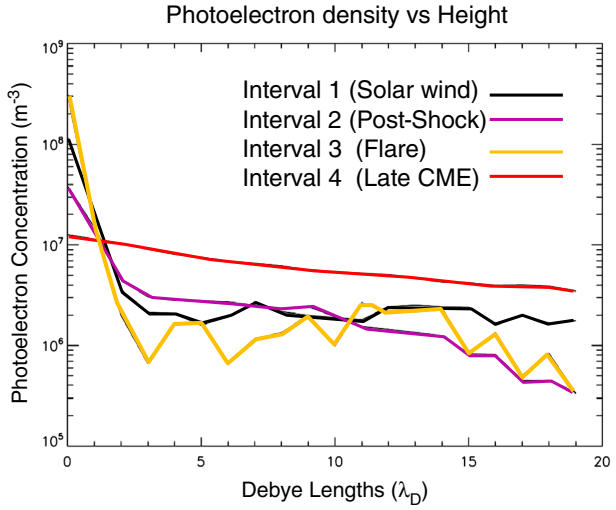

Figure 3. The photoelectron density from the F code run after 36 plasma periods for the four intervals examined in the study. The ability of photoelectrons to escape the near-surface increases as J_e increases, with intervals 2 and 4 with the lowest concentration of trapped photoelectrons. Note that 1 $\lambda_D \sim 10$ m in the solar wind

exclusively to trapping. However, the inward directed E-field region between 3 and 30 m in height acts to accelerate the electrons. In this region, there is an additional density decrease from 3 to 30 m due to conservation of flux; e.g., the increase in photoelectron velocity further reduces the photoelectron density.

[20] We do indeed note that there is photoelectron escape from the surface (beyond the 3 m trapping region), although not substantially, to form a precursor region many tens of meters in altitude. The density is reduced due to both trapping and acceleration of electrons in this non-monotonic potential.

5. Interval 2: Post-Shock Plasma Region

[21] As shown in Figure 1, during the post-shocked plasma passage (interval 2), the solar wind electron density increases by nearly a factor of ~4. Also, the electron temperature increases by a factor of ~2–3. Given the presence of the dense warm solar wind electrons, the ratio J_p/J_e decreases substantially compared to the nominal solar wind, to values of ~0.5.

[22] As evident in Figure 2a, the near-surface potential during this time is very different than the nominal solar wind (interval 2, purple line). In fact the monotonic potential appears similar to a typical Debye sheath where the surface is charging negative due to the presence of the incoming warm, post-shocked electron currents. These incoming solar wind currents decrease the surface potential (to negative values) which effectively acts to accelerate all photoelectrons away from the surface.

[23] This repulsion is clearly evident in the photoelectron density profiles. The surface density is about $5 \times 10^7/m^3$. However, at about 10 m in height, the photoelectrons reach their upstream density of about $2 \times 10^7/m^3$, making the ratio of surface-to-upstream photoelectron density only about a factor of ~2.5. Furthermore, this change in density is not due to trapping but is strictly the result of conservation of flux as the photoelectrons are accelerated in the strongly negative potential (inward directed E-field region) between 0 and 30 m in height.

6. Interval 3: Early CME Period

[24] As shown in Figure 1, after being in the post-shocked plasma for about 8 h, the Moon passed through a MHD discontinuity and into the medium containing the CME driver gas. Early in this period, the plasma has a density and temperature structure comparable to the solar wind case in interval 1. As such, we refer to interval 1 as representative of the solar wind and photoelectrons during this time period.

7. Interval 4: Late CME Period

[25] Near the start of 3 May 1998, the CME driver gas became highly concentrated, with a density of over 10 times that of the nominal solar wind. This CME plasma is cool, with a temperature of about one fourth that of the nominal solar wind case (~2–3 eV). The ratio of J_p/J_e is now 0.6, with J_e being a high density cool plasma—the current is increased by the larger number of electrons.

[26] Figure 2a shows the potential as a function of altitude for this case (interval 4, red line). There are two unexpected results for this case: First, the surface charges slightly positive, to a value of +1 V. For a photoelectron Maxwellian distribution with a temperature of 2.2 eV, most of the electrons will escape this potential, but not all of them. Hence, there is some electrostatic trapping in the near-surface region. Second, there is no region above the surface where the E field is directed inward (or where the potential dips negative). Hence, the potential structure in this case is monotonic in nature.

[27] Figure 2b shows the associated photoelectron density profile for the late CME/interval 4 time period. Like the post-shock plasma when $J_p/J_e < 1$ (interval 2), the density is nearly constant with altitude. At the surface, photoelectron concentrations are at $10^8/m^3$ but drop only to $4 \times 10^7/m^3$ in the distant upstream region. The ratio of surface-to-upstream photoelectron density is ~2.5. From the potential profile, we note that the electrons are not accelerated outward during this case, and the density increase at the surface is due to the slight positive potential which acts to trap the slower-moving electrons at the surface (in the first few meters).

[28] We note in intervals 2 and 4, both cases have $J_p/J_e \sim 0.5$ and the solar wind electron current exceeds the photoelectron current. In both cases, the ratio of photoelectron surface-to-upstream density ratio is about 2.5. However, the physical processes creating the similar ratios differ in each case. In interval 2, a classic sheath structure develops as a result from the warmer electron population, with $T_e \gg T_p$. The photoelectrons are then accelerated in the large region of negative potential, with flux conservation dictating the final surface-to-upstream photoelectron density ratio.

[29] However, in interval 4, we have a situation where J_p is ~4 μA/m^2, J_e is ~7 μA/m^2, but the ion flux, J_i, is now close to 4 μA/m^2 (the ion flow is ~500 km/s and the density is close to 50 ions per cm^3). The combination of J_p and J_i (both inward currents) sums to slightly greater values than J_e (outward current) resulting in a slightly positively charged surface at approximately +1 V potential. This effect leads

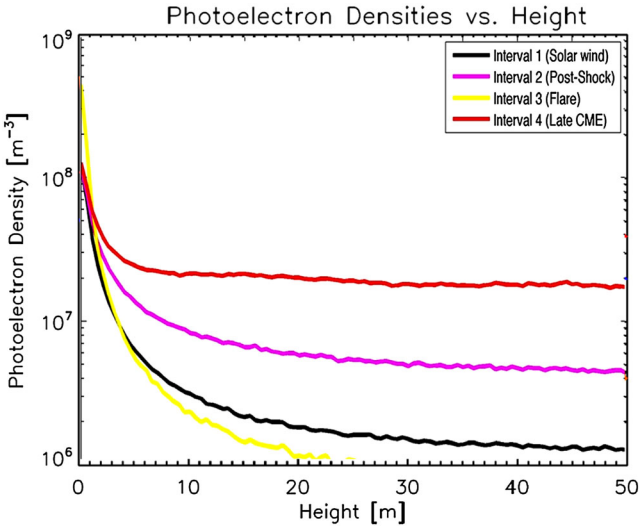

Figure 4. The photoelectron density from the Z code for the four intervals examined in the study. The ability of photoelectrons to escape the near-surface increases as J_e increases, with intervals 2 and 4 with the greatest photoelectron escape into upstream regions.

to the unexpected situation that there is near-surface trapping for this high-density case, creating the surface-to-upstream photoelectron density ratio of 2.5. Ironically, the photoelectron density ratios are the same for the interval 2 (warm) and interval 4 (cold) cases, but the underlying physical processes creating the result appear to be different (discussed more in section 9).

8. Return to Interval 3: Anomalous Flare Event

[30] As stated above, the plasma content of interval 3/early CME was mostly unremarkable, with thermal electron current levels comparable to the nominal solar wind. However, an unusual event did occur in the middle of this prosaic interval: An X1 solar flare was active on the Sun at 13:13 UT on 2 May 1998. During such flares, there is an increase in X-ray and EUV flux at the Moon that is expected to increase the photoelectric density by a factor of 5 [*Poppe and Horanyi*, 2010, and references therein]. While we do not have access to a surface monitor to determine the true photoelectron flux increase, we simulated this effect by increasing the photoelectron beam density by a factor of 5 in the simulations. In this case, J_p now exceeds J_e by nearly a factor of 20, and we anticipate an even stronger beam trapping region.

[31] Figure 2a shows a potential profile (interval 3a, yellow) that is non-monotonic, with a surface potential of close to +7 V and a −1.5 V minimum located at about 8 m in height. For a photoelectron Maxwellian distribution with T_p of 2.2 V, the +7 V potential is over three photoelectron temperatures (3 sigma) in size, and only those few electrons contained in the high-energy tail of the distribution are thus allowed to propagate upstream.

[32] This result is consistent with the density profile in Figure 2b, where the surface photoelectron density is close to $5 \times 10^8/m^3$ but has a reduced value of $4 \times 10^6/m^3$ in distant regions, making the surface-to-upstream photoelectron density ratio near 125. In the first 3 m from the surface, the E field is directed outward and this "electrically" contains a large portion of the photoelectrons. From 3 to 30 m in altitude, the E field is directed inward, and those few photoelectrons that do escape are now accelerated outward. The photoelectron density from 3 to 30 m continues to decrease but now due solely to the conservation of flux.

[33] There is a certain irony that the photoelectric sheath is in its strongest configuration during this time, fully capable of trapping/containing nearly all of the emitted photoelectrons to the near-surface region. Yet, within just 6 h (in just 1% of a lunation), the trapping sheath region disappears and the surface is in its most open configuration in interval 4. Clearly, the passage of a CME during the solar active period in early May 1998 creates extreme morphologies in the dayside lunar photoelectric sheath.

9. Comparison to Other Simulations

[34] The simulation results shown in Figure 2 were derived from a 1-D particle-in-cell code used in *Poppe and Horanyi* [2010]. Because the study involves an investigation of parameter space that is newly explored, we compare this code's results to a set of the results from two other 1-D PIC codes having slightly different boundary conditions and start-up processes for validation of the overall trapping/escaping effect. The other two codes, described in section 3, include one developed in the mid-1980s [*Farrell et al.*, 1989] and a 1-D code developed to confirm more advanced 2-D PIC simulations of plasma expansion into voids [*Zimmerman et al.*, 2011]. We will refer to these codes as PH, F, and Z, respectively, to differentiate the codes by their authors' names. The PH code presents the primary results, with the F and Z code results providing critical validation. In each code, the inner boundary is modeled as a solid surface. However, the outer boundary is treated differently in the models. In the PH code, any photoelectrons or plasma particles leaving that boundary are placed back into the system as solar wind plasma, and in the Z code, a constant flux of solar wind particles is injected into the simulation through the open boundary independently of the details of the outflowing population. In contrast, the F code has an open outer boundary: Plasma from a large reservoir initially fills a domain from the inner boundary ($X = 0\ \lambda_D$) to 3 times the simulation box length ($X = 300\ \lambda_D$) and streams inward toward the lunar boundary. The electrical effects are considered within the domain of the "box" with the plasma streaming ballistically from $100\ \lambda_D < X < 300\ \lambda_D$ based on their initial thermal and flow speed. Eventual reservoir depletion and escaping photoelectrons (moving beyond $X > 100\ \lambda_D$) create a system-level charge imbalance and at this point the simulation is turned off. The use of the reservoir maintains E = 0 across the outer boundary without the need for recycling plasma. However, the F code can only be run for relatively short periods of time while the PH and Z codes can be run for long periods.

[35] Different start-up conditions are simulated as well. At the simulation start-up, the PH code releases solar wind plasma from the outer boundary to drift inward and releases photoelectrons from the inner boundary to propagate outward. As such, there is settling time required as solar wind plasma propagates across the box and establishes equilibrium with the inner surface/wall. In contrast, the F and Z

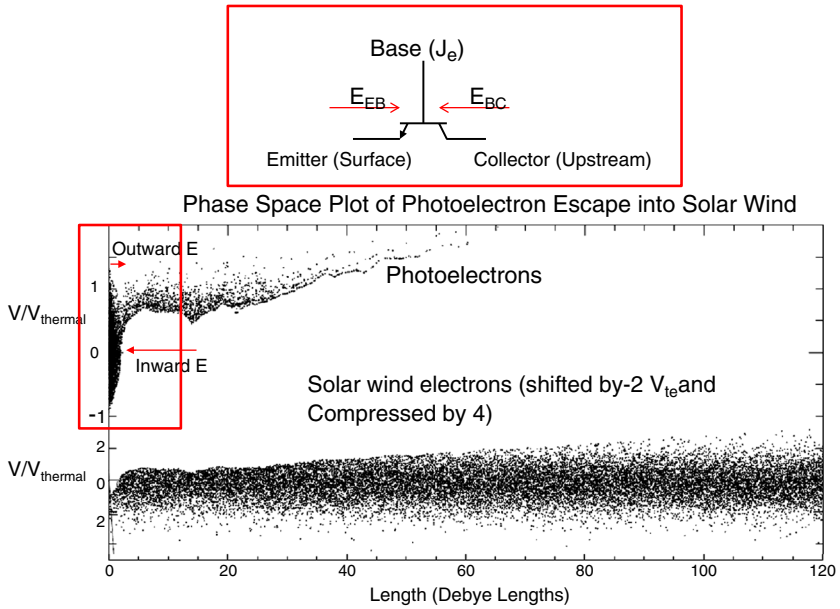

Figure 5. An example of the phase space X versus V configuration for the escaping photoelectrons and incoming solar wind for interval 1 (nominal solar wind) from the F code. To differentiate the two electron populations in the figure, the solar wind electrons have been shifted in velocity and velocity compressed (only for illustrative purposes). The top of the figure shows an electrical analog: the transistor. This device also has two E-field regions that electrons must cross in order to flow from left to right, and the potential drop is controlled by an external current. The transistor flow is considered "off" when E_{EB} is pointing to the right, much like the photoelectron flow is considered "off" when the near-surface E points to the right.

codes start at $t=0$ with solar wind plasma immediately adjacent to the left boundary (surface) which allows the plasma to come into equilibrium with the wall very quickly (few plasma periods).

[36] We note there should be some caution in applying the term "equilibrium." Specifically, for the PH code, since solar wind plasma is released from one end of the system and photoelectrons are leased from the other end, there is a settling time for the "box" or system to achieve equilibrium (i.e., a box-level equilibrium). For the F and Z codes, the simulation commences with the solar wind plasma immediately adjacent to the surface boundary and comes to equilibrium with that boundary in a few plasma periods (plasma/surface equilibrium). As such, there is inherent difficulty in a direct comparison of results at identical times early in the simulation runs. However, over the long term, the nature of near-surface trapping and photoelectron escape appears in a similar fashion in all three simulations.

[37] Figures 3 and 4 show the photoelectron density profile for the four intervals from the F and Z codes, respectively. The F code displays the densities after 36 plasma periods, after the photoelectron beam has traveled about ~35 Debye lengths. Table 1 lists the surface-to-upstream photoelectron density ratios for all intervals from the PH, F, and Z codes. While we do note that there are some differences in these ratios, the overall trend is the same—that there is less trapping and substantially more photoelectron escape in intervals 2 and 4 in each of the simulations. Even though there are structural differences in the three simulations, the fact that all three create similar trapping behavior confirms the effect.

[38] While not a perfect analog, there is some parallel between J_e's control of the sheath potential and that of the base current's control of emitter-collector transistor flow. In a transistor, there are two distinct E-field regions at the interfaces of the doped NPN material [*Smith*, 1980], and these E fields can be externally controlled to allow increased electron flow from the transistor's emitter to the collector. These potential drops are controlled by a base current. In the case of the lunar surface, there are also two distinct E-field regions: that near the surface from 0 to 3 m and a second region from 3 to 30 m in altitude, and these E-fields can be externally controlled to allow increased photoelectron flow from surface to upstream regions. The potential drops are controlled by J_e.

[39] Figure 5 shows a phase space velocity versus altitude diagram (V_x versus X) for the photoelectrons and solar wind electrons in interval 1, the nominal solar wind case. The figure also includes an illustration of a transistor. When a base current is applied that allows the voltage of the base to exceed that of the emitter, current will flow from emitter into the collector (the external E fields both point to the left in this case). For the lunar surface, this case is like interval 2 when J_e is large enough to reduce the surface potential, thereby allowing the two E fields to point to the left, creating an escaping and accelerating photoelectron population into upstream regions. For the transistor, if there is little current applied to the base and the base voltage drops below that of the emitter voltage (reverse biased), the external E field across the emitter and base junction (E_{EB}) now points to the right and acts to shut off the current (called the "transistor cutoff region"). For the lunar surface, this is the low J_e case, where the surface E now points outward (to the right) to create reduced upstream flow and a large trapping region.

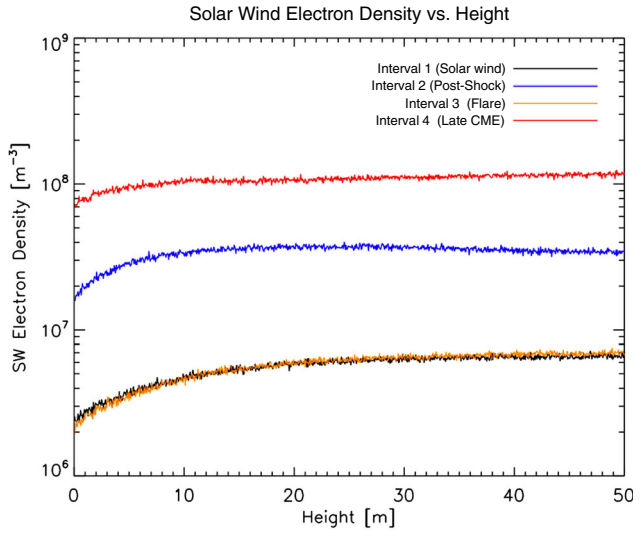

Figure 6. Solar wind electron density as a function of altitude from the PH simulation. The profiles are presented for each of the four intervals under study.

This case is illustrated in Figure 5. This base-controlled behavior of the transistor allows it to be considered a "switch," and we suggest, by analogy, that the lunar surface can switch from a trapped to a free-flowing configuration depending upon J_e. In nominal solar wind, the lunar surface is "off" and there is only an upstream leakage current, but during a solar storm, the lunar surface is "on" and large photoelectron currents now flow upstream.

[40] Figure 5 implies that there are really two potentials that develop near the lunar surface, as pictured in Figure 3 of *Nitter et al*. [1998]. Specifically, when no photoelectrons are emitted, a classic monotonic plasma sheath forms with increasing negative potential values as distance to the surface decreases. However, as photoelectron currents steadily increase, the surface develops an increase in potential that forms the non-monotonic sheath. At the subsolar point, $J_p > J_e$ and there is a positive near-surface potential that then creates an obvious non-monotonic signature. Thus, for $J_p < J_e$ (interval 2), the solar wind electron thermal flux greatly exceeds the photoelectron flux, making the surface negative in potential and thus creating a "traditional" monotonic sheath. However, for $J_p > J_e$ (intervals 1, 3, and 3a), the positive upswing in surface potential creates the non-monotonic structure.

[41] As described in section 7, interval 4 is an interesting case with J_e near 7 μA/m^2, J_p near 4 μA/m^2, and J_i near 4 μA/m^2. In the dense, colder plasma, the solar wind ion currents become a contributing factor. Specifically, there is slight more current inflowing toward that surface ($J_p + J_i$) than outflowing (J_e), thus the surface charges positive, but only slightly positive. However, J_i is now becoming comparable to J_e, making the Debye-like sheath potential structure at higher altitudes nearly nonexistent. There is no large excursion to negative potentials values in the region between 3 and 30 m. The combination of these summed potentials then acts to form a monotonic potential structure.

[42] All three simulations also noted a distinct alteration in the solar wind electron distributions inflowing to the boundary. The changes are represented in Figure 6 from the PH simulation (the F and Z simulation noted a nearly identical effect). Specifically, in all cases, the ambient solar wind electron density displayed a significant decrease with decreasing altitude. There are two reasons for this decrease: first, occultation/blocking of a large portion of the solar wind thermal electron population by the Moon itself (i.e., shadowing). The solar wind thermal electron velocity distribution has a substantial component flowing back toward the Sun (away from the Moon) and this outward directed flow is now occulted or blocked by the presence of the lunar surface. This leads to at least a 30% decrease in near-surface electron density. Second, the surface potentials also act to reflect solar wind electrons back upstream and account for the remainder of the near-surface decrease. In all cases, the solar wind ion inflow was constant and undisturbed.

[43] While the trend of photoelectron trapping and escape with J_e is similar between the three models, there are some differences of note. Specifically, the F model detected a strong boundary oscillation to the entire trapped sheath, similar to that reported in *Winglee and Pritchett* [1987], in conditions when $J_p/J_e > 1$. As described in *Winglee and Pritchett* [1987], the oscillation was due to the impulsive buildup and release of trapped photoelectron beams in a set of "fronts." As photoelectrons are ejected from a surface in a strong positive potential, a large fraction are physically "sucked" back to the surface (i.e., have negative velocities in the sheath) to become incident with the surface. This photoelectron return current temporarily reduced the trapping potential, thereby allowing a photoelectron beam "bunch" or front to escape outward away from the sheath. These fronts eventually coalesce to create the escaping photoelectron population. Because the F simulation models early times with the plasma adjacent to the surface, this oscillation may have been more apparent in this simulation. Further investigation of this effect will be presented in future work.

10. Conclusions

[44] The highly variable CME plasma conditions create a quick change in the solar wind electron thermal flux incident on the lunar surface, effectively varying the controlling solar wind electron thermal flux in a short time period. During the CME passage, J_p/J_e is highly variable jumping from values in a range from 0.5 to 20 on the time scale of tens of hours. In nominal solar wind, $J_p > J_e$ and a sheath trapping region forms that is strong and contains a concentration that is 30 times greater than that found in upstream regions. However, when the dayside lunar surface is exposed to the post-shocked plasma or late CME plasma, $J_p < J_e$ and the sheath region effectively disappears to allow a (mostly) free flow of photoelectrons into the upstream region. Ironically, a few hours before the late CME, a solar flare occurred that should have produced $J_p/J_e \sim 20$, and we find that such an environment will create strongly trapped surface photoelectron concentrations that are >100 times greater than that found in upstream regions. The transition from a trapped to escaping photoelectric sheath occurs when $J_p \sim J_e$, and this transition occurs at the fast-changing boundaries between intervals 1 and 2, intervals 2 and 3, and intervals 3 and 4. For nominal solar wind density ($n_e \sim 5 \times 10^6$/m^3), the temperature has to increase to 60 eV to have $J_p \sim J_e$, or for nominal solar wind temperatures (~10 eV), the solar wind density has to increase to 14×10^6/m^3 to have $J_p \sim J_e$.

[45] In cases where non-monotonic potentials form, like in intervals 1 and 3, the surface region of outward E and higher altitude region of inward E both act to reduce the overall escaping photoelectron density. The near-surface region acts to trap lower energy electrons and those few that do escape the surface potential are accelerated by the inward E at higher altitudes to further reduce density values based on the conservation of flux. We draw a rough analogy to the photoelectron region and transistor behavior.

[46] As evident in Figures 2b and 3, during the late CME passage, the photoelectron densities in the upstream region are many times greater than in the nominal solar wind. These outward streaming field-aligned electrons form a precursor layer that can be detected in distant regions from the Moon [*Halekas et al*., 2012a, 2012b] and, while the CME driving plasma passes, the precursor layer should "thicken" with electrons. These electrons may initiate a wave-particle interaction that provides wave turbulence that then acts to slow the incoming solar wind plasma. Future simulations can move the picture herein from the local (~50 m) to the distant.

[47] Finally, compared to a lunation, the time scale of variations to the dayside sheath potential is relatively fast, going from a trapped to escaping configuration (and back again) on time scales of tens of hours. In essence, the change in solar wind electron thermal currents, J_e, acts like a control or switch that varies the strength of the near-surface photoelectron trapping potential in cadence with the dynamic prevailing extreme space weather conditions. We also note that the processes described here apply to any exposed rocky body, like an asteroid. Certainly, along connecting dayside magnetic field lines, we should expect leaking photoelectrons, and their release will also be a function of the critical J_p/J_e ratio.

References

Angelopoulos, V. (2011), The ARTEMIS mission, *Space Sci. Rev.*, *165*, 3.

Farrell, W. M., and C. K. Goertz (1990), The coherent Cerenkov radiated power from a group of field-aligned test particles in a magnetoplasma, *Planet. Space Sci.*, *38*, 373.

Farrell, W. M., et al. (1989), Coherent Cerenkov emission from the Spacelab-2 electron beam, *J. Geophys. Res.*, *94*, 443.

Farrell, W. M., et al. (2012), Solar-Storm/Lunar Atmosphere Model (SSLAM): An overview of the effort and description of the driving storm environment, *J. Geophys. Res.*, *117*, E00K04, doi:10.1029/2012JE004070.

Feuerbacher, B., et al. (1972), Photoemission from the lunar surface fines and the lunar photoelectron sheath, Proceedings of the Third Lunar Science Conference, Supplement 3, *Geochim. Cosmochim. Acta*, *3*, 2655.

Halekas, J. S., S. D. Bale, D. L. Mitchell, and R. P. Lin (2005), Electrons and magnetic fields in the lunar plasma wake, *J. Geophys. Res.*, *110*, A07222, doi:10.1029/2004JA010991.

Halekas, J. S., G. T. Delory, W. M. Farrell, V. Angelopoulos, J. P. McFadden, J. W. Bonnell, M. O., Fillingim, and F. Plaschke (2011), First remote measurements of lunar surface charging from ARTEMIS: Evidence for non-monotonic sheath potentials above the dayside surface, *J. Geophys. Res.*, *116*, A07103, doi:10.1029/2011JA016542.

Halekas, J. S., A. Poppe, G. T. Delory, W. M. Farrell, and M. Horanyi (2012a), Solar wind electron interaction with the dayside lunar surface and crustal magnetic fields: Evidence for precursor effects, *Earth Planets Space*, *64*, 73–82.

Halekas, J. S., et al. (2012b), Lunar precursor effects in the solar wind and terrestrial magnetosphere, *J. Geophys. Res.*, *117*, A05101, doi:10.1029/2011JA017289.

Manka, R. H. (1973), Plasma and potential at the lunar surface, in *Photon and Particle Interactions With Surfaces in Space*, edited by R. J. L. Grard, pp. 347–361, D., Reidel, Dordrecht, Netherlands.

Nitter, T., O. Havnes, and F. Melandsø (1998), Levitation and dynamics of charged dust in the photoelectron sheath above surfaces in space, *J. Geophys. Res.*, *103*, 6605–6620, doi:10.1029/97JA03523.

Poppe, A., and M. Horányi (2010), Simulations of the photoelectron sheath and dust levitation on the lunar surface, *J. Geophys. Res.*, *115*, A08106, doi:10.1029/2010JA015286.

Poppe, A., J. S. Halekas, and M. Horanyi (2011), Negative potentials above the day-side lunar surface in the terrestrial plasma sheet: Evidence of non-monotonic potentials, *Geophys. Res. Lett.*, *38*, L02103, doi:10.1029/2010GL046119.

Poppe, A. R., et al., (2012), A comparison of ARTEMIS observations and particle-in-cell modeling of the lunar photoelectron sheath in the terrestrial magnetotail, *Geophys. Res. Lett.*, *39*, L01102, doi:10.1029/2011GL050321.

Reasoner, D. L., and W. J. Burke (1972a), Characteristics of the lunar photoelectron layer in the geomagnetic tail, *J. Geophys. Res.*, *77*, 6671.

Reasoner, D. L., and W. J. Burke (1972b), Direct observations of the lunar photoelectron layer, Proceedings of the Third Lunar Science Conference, Supplement 3, *Geochim. Cosmochim. Acta*, *3*, 2639.

Saito, Y., et al. (2008), Solar wind proton reflection at the lunar surface: Low energy ion measurement by MAP-PACE onboard SELENE (KAGUYA), *Geophys. Res. Lett.*, *35*, L24205, doi:10.1029/2008GL036077.

Smith, R. J. (1980), *Electronics: Circuits and Devices*, p. 152, John Wiley and Sons Inc, New York.

Stubbs, T. J., et al. (2006), A dynamic fountain model for lunar dust, *Adv. Space Res.*, *37*, 59.

Winglee, R. M., and P. L. Pritchett (1987), Space charge effects during injection of dense electron beams into space plasma, *J. Geophys. Res.*, *92*, 6114.

Zimmerman, M. I., et al., (2011), Solar wind access to lunar polar craters: Feedback between surface charging and plasma expansion, *Geophys. Res. Lett.*, *38*, L19202, doi:10.1029/2011GL048880.